

# A Hybrid AC/DC Microgrid and Its Coordination Control

Xiong Liu, *Student Member, IEEE*, Peng Wang, *Member, IEEE*, and Poh Chiang Loh, *Member, IEEE*

**Abstract**—This paper proposes a hybrid ac/dc micro grid to reduce the processes of multiple dc–ac–dc or ac–dc–ac conversions in an individual ac or dc grid. The hybrid grid consists of both ac and dc networks connected together by multi-bidirectional converters. AC sources and loads are connected to the ac network whereas dc sources and loads are tied to the dc network. Energy storage systems can be connected to dc or ac links. The proposed hybrid grid can operate in a grid-tied or autonomous mode. The coordination control algorithms are proposed for smooth power transfer between ac and dc links and for stable system operation under various generation and load conditions. Uncertainty and intermittent characteristics of wind speed, solar irradiation level, ambient temperature, and load are also considered in system control and operation. A small hybrid grid has been modeled and simulated using the Simulink in the MATLAB. The simulation results show that the system can maintain stable operation under the proposed coordination control schemes when the grid is switched from one operating condition to another.

**Index Terms**—Energy management, grid control, grid operation, hybrid microgrid, PV system, wind power generation.

## I. INTRODUCTION

THREE PHASE ac power systems have existed for over 100 years due to their efficient transformation of ac power at different voltage levels and over long distance as well as the inherent characteristic from fossil energy driven rotating machines. Recently more renewable power conversion systems are connected in low voltage ac distribution systems as distributed generators or ac micro grids due to environmental issues caused by conventional fossil fueled power plants. On other hand, more and more dc loads such as light-emitting diode (LED) lights and electric vehicles (EVs) are connected to ac power systems to save energy and reduce CO<sub>2</sub> emission. When power can be fully supplied by local renewable power sources, long distance high voltage transmission is no longer necessary [1]. AC micro grids [2]–[5] have been proposed to facilitate the connection of renewable power sources to conventional ac systems. However, dc power from photovoltaic (PV) panels or fuel cells has to be converted into ac using dc/dc boosters and dc/ac inverters in order to connect to an ac grid. In an ac grid, embedded ac/dc and dc/dc converters are required for various home and office facilities to supply different dc voltages. AC/DC/AC converters are commonly used as drives in order to control the speed of ac motors in industrial plants.

Manuscript received June 28, 2010; revised November 07, 2010; accepted February 12, 2011. Date of publication March 17, 2011; date of current version May 25, 2011. Paper no. TSG-00085-2010.

The authors are with the School of EEE, Nanyang Technological University, Singapore 639798, (e-mail: liux0039@e.ntu.edu.sg; epwang@ntu.edu.sg; ep-cloh@ntu.edu.sg).

Digital Object Identifier 10.1109/TSG.2011.2116162

Recently, dc grids are resurging due to the development and deployment of renewable dc power sources and their inherent advantage for dc loads in commercial, industrial and residential applications. The dc microgrid has been proposed [6]–[10] to integrate various distributed generators. However, ac sources have to be converted into dc before connected to a dc grid and dc/ac inverters are required for conventional ac loads.

Multiple reverse conversions required in individual ac or dc grids may add additional loss to the system operation and will make the current home and office appliances more complicated.

The smart grid concept is currently prevailing in the electric power industry. The objective of constructing a smart grid is to provide reliable, high quality electric power to digital societies in an environmentally friendly and sustainable way. One of most important futures of a smart grid is the advanced structure which can facilitate the connections of various ac and dc generation systems, energy storage options, and various ac and dc loads with the optimal asset utilization and operation efficiency. To achieve those goals, power electronics technology plays a most important role to interface different sources and loads to a smart grid.

A hybrid ac/dc microgrid is proposed in this paper to reduce processes of multiple reverse conversions in an individual ac or dc grid and to facilitate the connection of various renewable ac and dc sources and loads to power system. Since energy management, control, and operation of a hybrid grid are more complicated than those of an individual ac or dc grid, different operating modes of a hybrid ac/dc grid have been investigated. The coordination control schemes among various converters have been proposed to harness maximum power from renewable power sources, to minimize power transfer between ac and dc networks, and to maintain the stable operation of both ac and dc grids under variable supply and demand conditions when the hybrid grid operates in both grid-tied and islanding modes. The advanced power electronics and control technologies used in this paper will make a future power grid much smarter.

## II. SYSTEM CONFIGURATION AND MODELING

### A. Grid Configuration

Fig. 1 shows a conceptual hybrid system configuration where various ac and dc sources and loads are connected to the corresponding dc and ac networks. The ac and dc links are connected together through two transformers and two four-quadrant operating three phase converters. The ac bus of the hybrid grid is tied to the utility grid.

A compact hybrid grid as shown in Fig. 2 is modeled using the Simulink in the MATLAB to simulate system operations and controls. Forty kW PV arrays are connected to dc bus through

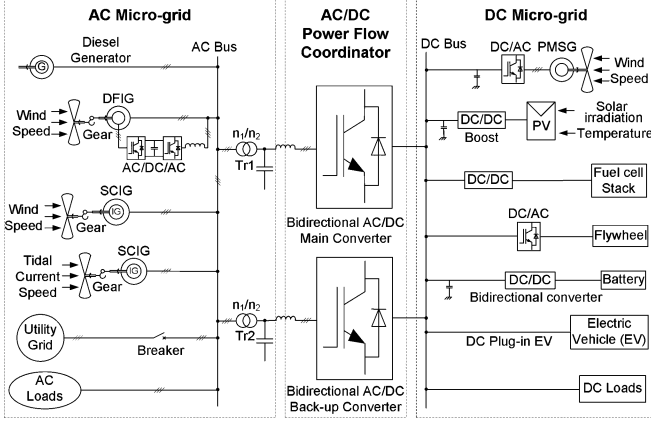


Fig. 1. A hybrid ac/dc microgrid system.

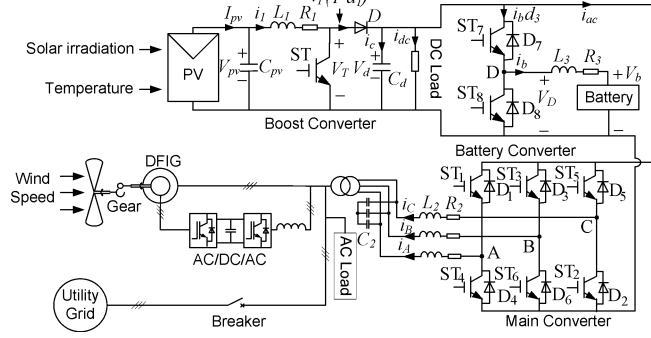


Fig. 2. A compact representation of the proposed hybrid grid.

a dc/dc boost converter to simulate dc sources. A capacitor  $C_{pv}$  is to suppress high frequency ripples of the PV output voltage. A 50 kW wind turbine generator (WTG) with doubly fed induction generator (DFIG) is connected to an ac bus to simulate ac sources. A 65 Ah battery as energy storage is connected to dc bus through a bidirectional dc/dc converter. Variable dc load (20 kW–40 kW) and ac load (20 kW–40 kW) are connected to dc and ac buses respectively. The rated voltages for dc and ac buses are 400 V and 400 V rms respectively. A three phase bidirectional dc/ac main converter with R-L-C filter connects the dc bus to the ac bus through an isolation transformer.

### B. Grid Operation

The hybrid grid can operate in two modes. In grid-tied mode, the main converter is to provide stable dc bus voltage and required reactive power and to exchange power between the ac and dc buses. The boost converter and WTG are controlled to provide the maximum power. When the output power of the dc sources is greater than the dc loads, the converter acts as an inverter and injects power from dc to ac side. When the total power generation is less than the total load at the dc side, the converter injects power from the ac to dc side. When the total power generation is greater than the total load in the hybrid grid, it will inject power to the utility grid. Otherwise, the hybrid grid will receive power from the utility grid. In the grid tied mode, the battery converter is not very important in system operation because power is balanced by the utility grid. In autonomous

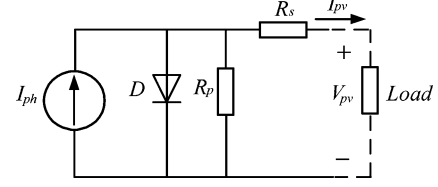


Fig. 3. Equivalent circuit of a solar cell.

TABLE I  
PARAMETERS FOR PHOTOVOLTAIC PANEL

Symbol	Description	Value
$V_{oc}$	Rated open circuit voltage	403 V
$I_{ph}$	Photocurrent	
$I_{sat}$	Module reverse saturation current	
$q$	Electron charge	$1.602 \times 10^{-19} C$
$A$	Ideality factor	1.50
$k$	Boltzman constant	$1.38 \times 10^{-23} J/K$
$R_s$	Series resistance of a PV cell	
$R_p$	parallel resistance of a PV cell	
$I_{sso}$	Short-circuit current	3.27 A
$k_i$	SC current temperature coefficient	$1.7e^{-3}$
$T_r$	Reference temperature	301.18 K
$I_{rr}$	Reverse saturation current at $T_r$	$2.0793e^{-6} A$
$E_{gap}$	Energy of the band gap for silicon	1.1eV
$n_p$	Number of cells in parallel	40
$n_s$	Number of cells in series	900
$S$	Solar radiation level	0~1000 W/m <sup>2</sup>
$T$	Surface temperature of the PV	350 K

mode, the battery plays a very important role for both power balance and voltage stability. Control objectives for various converters are dispatched by energy management system. DC bus voltage is maintained stable by a battery converter or boost converter according to different operating conditions. The main converter is controlled to provide a stable and high quality ac bus voltage. Both PV and WTG can operate on maximum power point tracking (MPPT) or off-MPPT mode based on system operating requirements. Variable wind speed and solar irradiation are applied to the WTG and PV arrays respectively to simulate variation of power of ac and dc sources and test the MPPT control algorithm.

### C. Modeling of PV Panel

Fig. 3 shows the equivalent circuit of a PV panel with a load. The current output of the PV panel is modeled by the following three equations [11], [12]. All the parameters are shown in Table I:

$$I_{pv} = n_p I_{ph} - n_p I_{sat} \times \left[ \exp \left( \left( \frac{q}{AkT} \right) \left( \frac{V_{pv}}{n_s} + I_{pv} R_s \right) \right) - 1 \right] \quad (1)$$

$$I_{ph} = (I_{sso} + k_i(T - T_r)) \cdot \frac{S}{1000} \quad (2)$$

$$I_{sat} = I_{rr} \left( \frac{T}{T_r} \right)^3 \exp \left( \left( \frac{qE_{gap}}{kA} \right) \cdot \left( \frac{1}{T_r} - \frac{1}{T} \right) \right) \quad (3)$$

### D. Modeling of Battery

Two important parameters to represent state of a battery are terminal voltage  $V_b$  and state of charge (SOC) as follows [13]:

TABLE II  
PARAMETERS OF DFIG

Symbol	Description	Value
$P_{nom}$	Nominal power	50 kW
$V_{nom}$	Nominal voltage	400 V
$R_s$	Stator resistance	0.00706 pu
$L_s$	Stator inductance	0.171 pu
$R_r$	Rotor resistance	0.005 pu
$L_r$	Rotor inductance	0.156 pu
$L_m$	Mutual inductance	2.9 pu
$J$	Rotor inertial constant	3.1 s
$n_p$	Number of poles	6
$V_{dc\_nom}$	Nominal DC voltage of AC/DC/AC converter	800 V
$P_m$	Nominal mechanical power	45 kW

$$V_b = V_o + R_b \cdot i_b - K \frac{Q}{Q + \int i_b dt} + A \cdot \exp \left( B \int i_b dt \right) \quad (4)$$

$$SOC = 100 \left( 1 + \frac{\int i_b dt}{Q} \right) \quad (5)$$

where  $R_b$  is internal resistance of the battery,  $V_o$  is the open circuit voltage of the battery,  $i_b$  is battery charging current,  $K$  is polarization voltage,  $Q$  is battery capacity,  $A$  is exponential voltage, and  $B$  is exponential capacity.

#### E. Modeling of Wind Turbine Generator

Power output  $P_m$  from a WTG is determined by (6)

$$P_m = 0.5 \rho A C_p(\lambda, \beta) V_w^3 \quad (6)$$

where  $\rho$  is air density,  $A$  is rotor swept area,  $V_w$  is wind speed, and  $C_p(\lambda, \beta)$  is the power coefficient, which is the function of tip speed ratio  $\lambda$  and pitch angle  $\beta$ .

The mathematical models of a DFIG are essential requirements for its control system. The voltage equations of an induction motor in a rotating  $d$ - $q$  coordinate are as follows:

$$\begin{bmatrix} u_{ds} \\ u_{qs} \\ u_{dr} \\ u_{qr} \end{bmatrix} = \begin{bmatrix} -R_s & 0 & 0 & 0 \\ 0 & -R_s & 0 & 0 \\ 0 & 0 & R_r & 0 \\ 0 & 0 & 0 & R_r \end{bmatrix} \begin{bmatrix} i_{ds} \\ i_{qs} \\ i_{dr} \\ i_{qr} \end{bmatrix} + p \begin{bmatrix} \lambda_{ds} \\ \lambda_{qs} \\ \lambda_{dr} \\ \lambda_{qr} \end{bmatrix} + \begin{bmatrix} -\omega_1 \lambda_{qs} \\ \omega_1 \lambda_{ds} \\ -\omega_2 \lambda_{qr} \\ \omega_2 \lambda_{dr} \end{bmatrix} \quad (7)$$

$$\begin{bmatrix} \lambda_{ds} \\ \lambda_{qs} \\ \lambda_{dr} \\ \lambda_{qr} \end{bmatrix} = \begin{bmatrix} -L_s & 0 & L_m & 0 \\ 0 & -L_s & 0 & L_m \\ -L_m & 0 & L_r & 0 \\ 0 & -L_m & 0 & L_r \end{bmatrix} \begin{bmatrix} i_{ds} \\ i_{qs} \\ i_{dr} \\ i_{qr} \end{bmatrix} \quad (8)$$

The dynamic equation of the DFIG

$$\frac{J}{n_p} \frac{d\omega_r}{dt} = T_m - T_{em} \quad (9)$$

$$T_{em} = n_p L_m (i_{qs} i_{dr} - i_{ds} i_{qr}) \quad (10)$$

where the subscripts  $d$ ,  $q$ ,  $s$ , and  $r$  denote  $d$ -axis,  $q$ -axis, stator, and rotor respectively,  $L$  represents the inductance,  $\lambda$  is the flux linkage,  $u$  and  $i$  represent voltage and current respectively,  $\omega_1$  and  $\omega_2$  are the angular synchronous speed and slip speed respectively,  $\omega_2 = \omega_1 - \omega_r$ ,  $T_m$  is the mechanical torque,  $T_{em}$  is the electromagnetic torque and other parameters of DFIG are listed in Table II.

If the synchronous rotating  $d$ - $q$  reference is oriented by the stator voltage vector, the  $d$ -axis is aligned with the stator voltage vector while the  $q$ -axis is aligned with the stator flux reference frame. Therefore,  $\lambda_{ds} = 0$  and  $\lambda_{qs} = \lambda_s$ . The following equations can be obtained in the stator voltage oriented reference frame as [14]:

$$i_{ds} = -\frac{L_m}{L_s} i_{dr} \quad T_{em} = n_p \frac{L_m}{L_s} \lambda_s i_{dr} \quad \sigma = \frac{L_s L_r - L_m^2}{L_s L_r} \quad (11)$$

$$u_{dr} = R_r i_{dr} + \sigma L_r \frac{di_{dr}}{dt} - (\omega_1 - \omega_r)(L_m i_{qs} + L_r i_{qr}) \quad (12)$$

$$u_{qr} = R_r i_{qr} + \sigma L_r \frac{di_{qr}}{dt} + (\omega_1 - \omega_r)(L_m i_{ds} + L_r i_{dr}). \quad (13)$$

### III. COORDINATION CONTROL OF THE CONVERTERS

There are five types of converters in the hybrid grid. Those converters have to be coordinately controlled with the utility grid to supply an uninterrupted, high efficiency, and high quality power to variable dc and ac loads under variable solar irradiation and wind speed when the hybrid grid operates in both isolated and grid tied modes. The control algorithms for those converters are presented in this section.

#### A. Grid-Connected Mode

When the hybrid grid operates in this mode, the control objective of the boost converter is to track the MPPT of the PV array by regulating its terminal voltage. The back-to-back ac/dc/ac converter of the DFIG is controlled to regulate rotor side current to achieve MPPT and to synchronize with ac grid. The energy surplus of the hybrid grid can be sent to the utility system. The role of the battery as the energy storage becomes less important because the power is balanced by the utility grid. In this case, the only function of the battery is to eliminate frequent power transfer between the dc and ac link. The dc/dc converter of the battery can be controlled as the energy buffer using the technique [15]. The main converter is designed to operate bidirectionally to incorporate complementary characteristic of wind and solar sources [16], [17]. The control objectives of the main converter are to maintain a stable dc-link voltage for variable dc load and to synchronize with the ac link and utility system.

The combined time average equivalent circuit model of the booster and main converter is shown in Fig. 4 based on the basic principles and descriptions in [18] and [19] for booster and inverter respectively.

Power flow equations at the dc and ac links are as follows:

$$P_{pv} + P_{ac} = P_{dcL} + P_b \quad (14)$$

$$P_s = P_w - P_{acL} - P_{ac} \quad (15)$$

Control of battery in  
grid-connected mode

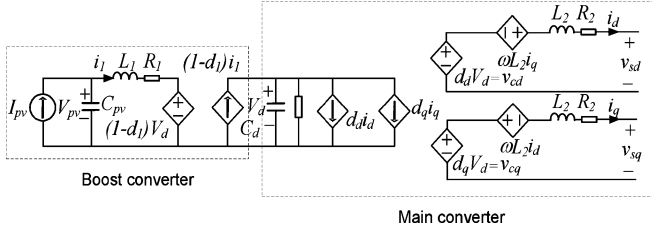


Fig. 4. Time average model for the booster and main converter.

where real power  $P_{pv}$  and  $P_w$  are produced by PV and WTG respectively,  $P_{acL}$  and  $P_{dcL}$  are real power loads connected to ac and dc buses respectively,  $P_{ac}$  is the power exchange between ac and dc links,  $P_b$  is power injection to battery, and  $P_s$  is power injection from the hybrid grid to the utility.

The current and voltage equations at dc bus are as follows:

$$V_{pv} - V_T = L_1 \cdot \frac{di_1}{dt} + R_1 i_1 \quad (16)$$

$$I_{pv} - i_1 = C_{pv} \cdot \frac{dV_{pv}}{dt} \quad (17)$$

$$V_T = V_d \cdot (1 - d_1) \quad (18)$$

$$i_1 (1 - d_1) - C_d \frac{dV_d}{dt} - \frac{1}{R_L} V_d - i_b - i_{ac} = 0 \quad (19)$$

where  $d_1$  is the duty ratio of switch ST.

Equations (20) and (21) show the ac side voltage equations of the main converter in ABC and  $d-q$  coordinates respectively [20]

$$L_2 \frac{d}{dt} \begin{bmatrix} i_A \\ i_B \\ i_C \end{bmatrix} + R_2 \begin{bmatrix} i_A \\ i_B \\ i_C \end{bmatrix} = \begin{bmatrix} v_{CA} \\ v_{CB} \\ v_{CC} \end{bmatrix} - \begin{bmatrix} v_{SA} \\ v_{SB} \\ v_{SC} \end{bmatrix} \quad (20)$$

$$L_2 \frac{d}{dt} \begin{bmatrix} i_d \\ i_q \end{bmatrix} = \begin{bmatrix} -R_2 & \omega L_2 \\ -\omega L_2 & -R_2 \end{bmatrix} \begin{bmatrix} i_d \\ i_q \end{bmatrix} + \begin{bmatrix} v_{cd} \\ v_{cq} \end{bmatrix} - \begin{bmatrix} v_{sd} \\ v_{sq} \end{bmatrix} \quad (21)$$

where  $(v_{CA}, v_{CB}, v_{CC})$  are ac side voltages of the main converter,  $(v_{SA}, v_{SB}, v_{SC})$  are voltages across  $C_2$  in Fig. 2, and  $(i_d, i_q)$ ,  $(v_{sd}, v_{sq})$  and  $(v_{cd}, v_{cq})$  are the corresponding  $d-q$  coordinate variables.

In order to maintain stable operation of the hybrid grid under various supply and demand conditions, a coordination control algorithm for booster and main converter is proposed based on basic control algorithms of the grid interactive inverter in [19]. The control block diagram is shown in Fig. 5.

The reference value of the solar panel terminal voltage  $V_{pv}^*$  is determined by the basic perturbation and observation (P&O) algorithm based on solar irradiation and temperature to harness the maximum power [21], [22]. Dual-loop control for the dc/dc boost converter is described in [23], where the control objective is to provide a high quality dc voltage with good dynamic response. This control scheme is applied for the PV system to track optimal solar panel terminal voltage using the MPPT algorithm with minor modifications. The outer voltage loop can guarantee voltage reference tracking with zero steady-state error and the inner current loop can improve dynamic response.

## How to set $i_{q\_ref}$ ?

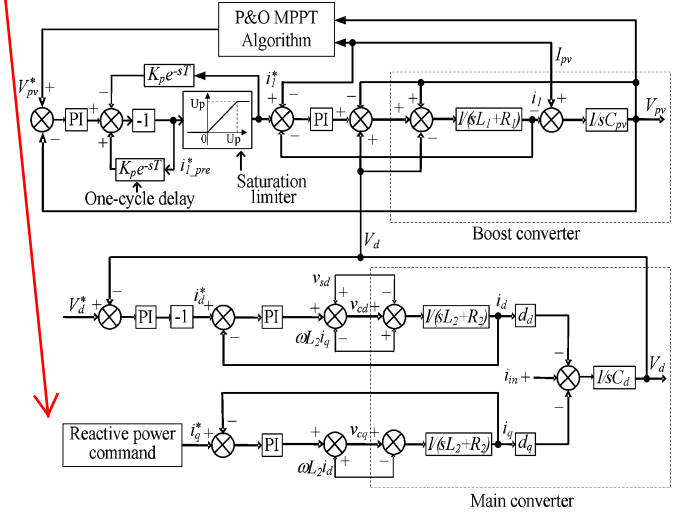


Fig. 5. The control block diagram for boost converter and main converter.

The one-cycle delay and saturation limiter in Fig. 5 can assist controller to track  $V_{pv}^*$  faster. In steady state,  $i_{1-pre}^*$  resides in the linear region of the saturation limiter and is equal to  $i_1^*$ . It can be seen that a step increase of  $V_{pv}^*$  makes  $i_{1-pre}^*$  becomes negative, which in turn makes  $i_1^*$  to be zero during the first switching period of the transient process. This leads to a lower  $d_1$  for driving the average voltage  $V_d(1 - d_1)$  and  $V_{pv}$  upward to follow the  $V_{pv}^*$  command.

To smoothly exchange power between dc and ac grids and supply a given reactive power to the ac link, PQ control is implemented using a current controlled voltage source for the main converter. Two PI controllers are used for real and reactive power control respectively. When resource conditions or load capacities change, the dc bus voltage is adjusted to constant through PI regulation. The PI controller is set as instantaneous active current  $i_d$  reference whereas the instantaneous reactive current  $i_q$  reference is determined by reactive power compensation command.

When a sudden dc load drop causes power surplus at dc side, the main converter is controlled to transfer power from the dc to the ac side. The active power absorbed by capacitor  $C_d$  leads to the rising of dc-link voltage  $V_d$ . The negative error  $(V_d^* - V_d)$  caused by the increase of  $V_d$  produces a higher active current reference  $i_d^*$  through the PI control. The active current  $i_d$  and its reference  $i_d^*$  are both positive. A higher positive reference  $i_d^*$  will force active current  $i_d$  to increase through the inner current control loop. Therefore, the power surplus of the dc grid can be transferred to the ac side.

Similarly, a sudden increase of dc load causes the power shortage and  $V_d$  drop at the dc grid. The main converter is controlled to supply power from the ac to the dc side. The positive voltage error  $(V_d^* - V_d)$  caused by  $V_d$  drop makes the magnitude of  $i_d^*$  increase through the PI control. Because  $i_d$  and  $i_d^*$  are both negative, the magnitude of  $i_d$  is increased through the inner current control loop. Therefore, power is transferred from the ac grid to the dc side.

The DFIG is controlled to maintain a stable dc-link voltage of the back-to-back ac/dc/ac converter. The objectives of the rotor-side converter are to track MPPT of the WTG and to manage the stator side reactive power. Different control schemes such as



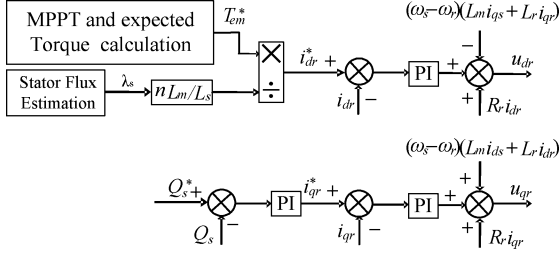


Fig. 6. The DTC control scheme for the rotor side converter.

the direct torque control (DTC) and direct power control (DPC) have been proposed for a DFIG in literature [24] and [14], [25]. The DTC scheme as shown in Fig. 6 is selected as the control method for the rotor side converter in this paper. The rotor rotational speed is obtained through the MPPT algorithm, which is based on the power and speed characteristic of the wind turbine [26]. The rotational speed  $\omega_r$  and mechanical power  $P_m$  are used to calculate the electromagnetic torque  $T_{em}^*$ . The  $d$ -axis rotor side current reference is determined based on  $T_{em}^*$  through stator flux estimation. The rotor side  $d$ - $q$  voltages are maintained through controlling the corresponding current with appropriate feed forward voltage compensation.

### B. Isolated Mode

When the hybrid grid operates in the islanding mode, the boost converter and the back-to-back ac/dc/ac converter of the DFIG may operate in the on-MPPT or off-MPPT based on system power balance and energy constraints. The main converter acts as a voltage source to provide a stable voltage and frequency for the ac grid and operates either in inverter or converter mode for the smooth power exchange between ac and dc links. The battery converter operates either in charging or discharging mode based on power balance in the system. The dc-link voltage is maintained by either the battery or the boost converter based on system operating condition. Powers under various load and supply conditions should be balanced as follows:

$$P_{pv} + P_w = P_{acL} + P_{dcL} + P_{loss} + P_b \quad (22)$$

where  $P_{loss}$  is the total grid loss.

Two level coordination controls are used to maintain system stable operation. At the system level, operation modes of the individual converters are determined by the energy management system (EMS) based on the system net power  $P_{net}$  and the energy constraints and the charging/discharging rate of battery. The system control logic diagram is shown in Fig. 7.  $P_{net}$  is defined as the total maximum power generation minus the total load and minus  $P_{loss}$ . The energy constraints of the battery are determined based on the state of charge (SOC) limits using  $SOC_{min} < SOC \leq SOC_{max}$ . It should be noted that SOC cannot be measured directly, but can be attained through some estimation methods as described in [27], [28]. The constraint of charging and discharging rate is  $P_b \leq P_{bmax}$ . At local level, the individual converters operate based on mode commands from the EMS. Either the PV system or WTG or both have to operate in the off-MPPT mode for Case 1 and Case 2 and in the

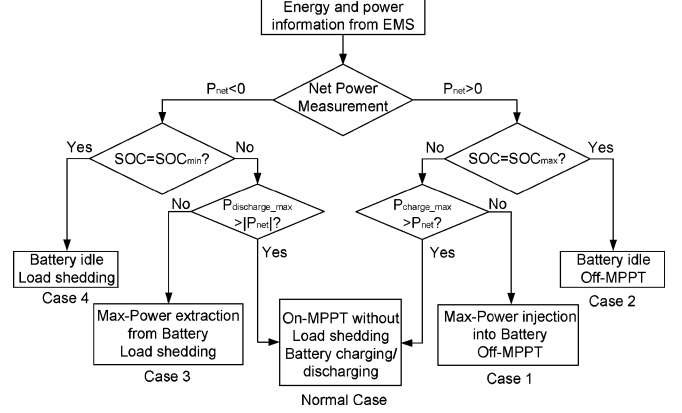


Fig. 7. Control mode diagram for the isolated hybrid grid.

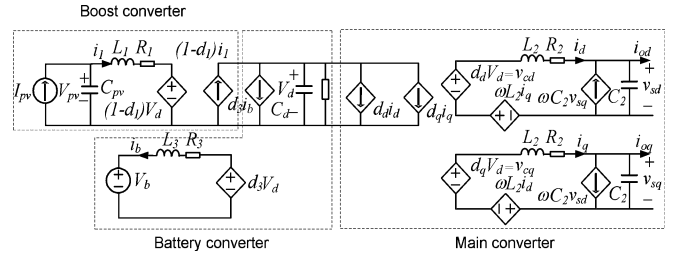


Fig. 8. Time average equivalent circuit model for the three converters.

on-MPPT mode for other cases. The battery converter may operate in the idle, charging, or discharging mode for different cases. The main converter will operate in the inverter mode if  $P_w - P_{acL}$  is negative or in the converter mode with positive  $P_w - P_{acL}$ . Load shedding is required to maintain power balance if power supply is less than demand and the battery is at the minimum SOC.

The time average equivalent circuit model of the booster, main converter, and battery converter for the isolated operation is shown in Fig. 8. The inverter part of the circuit model in Fig. 8 is based on the basic principles and descriptions in [29].

The current and voltage equations for the battery converter and dc link are as follows:

$$V_D - V_b = L_3 \cdot \frac{di_b}{dt} + R_3 i_b \quad (23)$$

$$V_D = V_d \cdot d_3 \quad (24)$$

$$i_1(1 - d_1) - i_{ac} - i_{dc} - i_b \cdot d_3 = i_c = C_d \cdot \frac{dV_d}{dt} \quad (25)$$

where  $d_3$  and  $(1 - d_3)$  are the duty ratio of the switches ST<sub>7</sub> and ST<sub>8</sub> respectively.

The ac side current equations of the main converter in  $d$ - $q$  coordinate are as follows:

$$C_2 \frac{d}{dt} \begin{bmatrix} v_{sd} \\ v_{sq} \end{bmatrix} = \begin{bmatrix} i_d \\ i_q \end{bmatrix} + \begin{bmatrix} 0 & \omega \\ -\omega & 0 \end{bmatrix} \begin{bmatrix} v_{sd} \\ v_{sq} \end{bmatrix} - \begin{bmatrix} i_{od} \\ i_{oq} \end{bmatrix} \quad (26)$$

where  $i_{od}$  and  $i_{oq}$  are  $d$ - $q$  currents at the converter side of the transformer respectively.

Multi-loop voltage control for a dc/ac inverter is described in [30], where the control objective is to provide a high quality ac voltage with good dynamic response at different load conditions. This control scheme can also be applied for main converter control to provide high quality ac voltage in

because  $i_b$  is defined positive when flowing into the battery

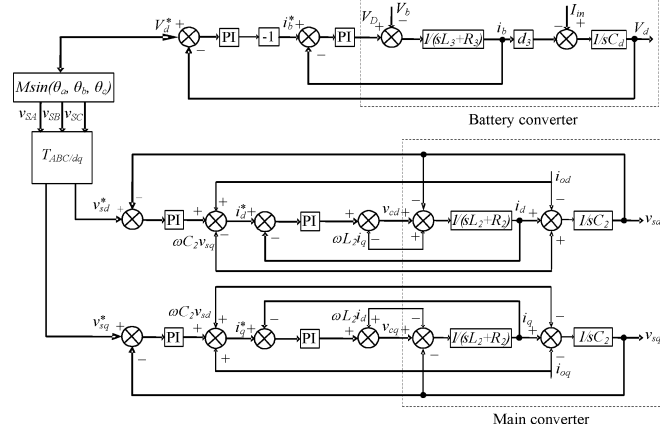


Fig. 9. Block diagram of the battery and main converters for the normal case.

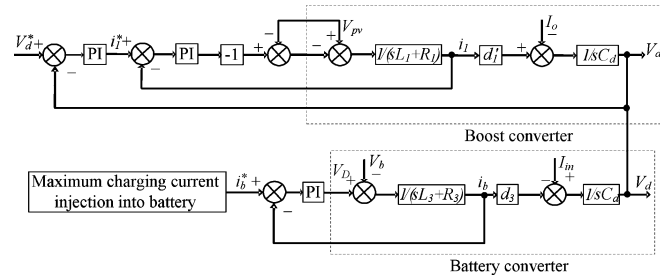


Fig. 10. Block diagram of the booster and battery converter for Case 1.

stand-alone mode with minor modifications. The coordinated control block diagram for the normal case is shown in Fig. 9. To provide a stable dc-link voltage, the dual loop control scheme is applied for the battery converter. The injection current  $I_{in} = i_1(1 - d_1) - i_{ac} - i_{dc}$ . It should be noted that the output of the outer voltage loop is multiplied by  $-1$  before it is set as the inner loop current reference. Current  $i_b$  is defined positive when flowing into the battery, where the preset dc-link voltage  $V_{dc}^*$  is set to constant 400 V. Considering a decrease of  $V_{dc}$  caused by sudden load increase or decrease of solar irradiation, the positive voltage error ( $V_{dc}^* - V_{dc}$ ) multiplied by  $-1$  through the PI produces a negative  $i_b^*$  for the inner current loop, which makes the battery to transfer from charging into discharging mode and to rise  $V_{dc}$  back to its preset value  $V_{dc}^*$ . The battery converter is transferred from discharging into charging mode in the similar control method. The main converter provides a stable ac bus voltage for the DFIG converter as shown in the bottom of Fig. 9.

The control objectives for the converters change when the system transfers from one operating scenario to another. For example, the role of the boost converter is changed to provide a stable dc-link voltage rather than the MPPT for cases 1 and 2, while the battery converter is controlled to absorb the maximum power in case 1 and is switched off in case 2. The coordinated control block diagram for these two converters in Case 1 is described in Fig. 10. The boost converter provides a stable dc-link voltage. The main converter is controlled to provide a stable ac bus voltage. The current  $I_o$  in Fig. 10 is equal to  $i_{ac} + i_{dc} + i_b d_3$  and  $d_1'$  is equal to  $(1 - d_1)$ .

The anti-islanding technique is one of the essential functions for reliable operation of distributed generation systems. Many anti-islanding detection and control schemes [31], [32] have

TABLE III  
COMPONENT PARAMETERS FOR THE HYBRID GRID.

Symbol	Description	Value
$C_{pv}$	Capacitor across the solar panel	110uF
$L_1$	Inductor for the boost converter	2.5mH
$C_d$	Capacitor across the dc-link	4700uF
$L_2$	Filtering inductor for the inverter	0.43mH
$R_2$	Equivalent resistance of the inverter	0.3ohm
$C_2$	Filtering capacitor for the inverter	60uF
$L_3$	Inductor for the Battery converter	3mH
$R_3$	Resistance of L3	0.1ohm
$f$	Frequency of the AC grid	60Hz
$f_s$	Switching frequency of power converters	10kHz
$V_d$	Rated DC bus voltage	400V
$V_{ll\_rms}$	Rated AC bus line voltage (rms value)	400V
$n_1/n_2$	Ratio of the transformer	2:1

been developed for conventional and power-converter-based distributed generators and various microgrids. Those techniques can be modified and implemented in the proposed hybrid grid to make the system transfer smoothly from the grid tied to isolated mode.

#### IV. SIMULATION RESULTS

The operations of the hybrid grid under various source and load conditions are simulated to verify the proposed control algorithms. The parameters of components for the hybrid grid are listed in Table III.

##### A. Grid-Connected Mode

In this mode, the main converter operates in the PQ mode. Power is balanced by the utility grid. The battery is fully charged and operates in the rest mode in the simulation. AC bus voltage is maintained by the utility grid and dc bus voltage is maintained by the main converter.

The optimal terminal voltage is determined using the basic P&O algorithm based on the corresponding solar irradiation. The voltages for different solar irradiations are shown in Fig. 11. The solar irradiation level is set as 400 W/m<sup>2</sup> from 0.0 s to 0.1 s, increases linearly to 1000 W/m<sup>2</sup> from 0.1 s to 0.2 s, keeps constant until 0.3 s, decreases to 400 W/m<sup>2</sup> from 0.3 s to 0.4 s and keeps that value until the final time 0.5 s. The initial voltage for the P&O is set at 250 V. It can be seen that the P&O is continuously tracing the optimal voltage from 0 to 0.2 s. The algorithm only finds the optimal voltage at 0.2 s due to the slow tracing speed. The algorithm is searching the new optimal voltage from 0.3 s and finds the optimal voltage at 0.48 s. It can be seen that the basic algorithm can correctly follow the change of solar irradiation but needs some time to search the optimal voltage. The improved P&O methods with fast tracing speed should be used in the PV sites with fast variation of solar irradiation.

Fig. 12 shows the curves of the solar radiation (radiation level times 30 for comparison) and the output power of the PV panel. The output power varies from 13.5 kW to 37.5 kW, which closely follows the solar irradiation when the ambient temperature is fixed.

Fig. 13 shows the voltage (voltage times 0.2 for comparison) and current responses at the ac side of the main converter when the solar irradiation level decreases from 1000 W/m<sup>2</sup> at 0.3 s to 400 W/m<sup>2</sup> at 0.4 s with a fixed dc load 20 kW. It can be seen

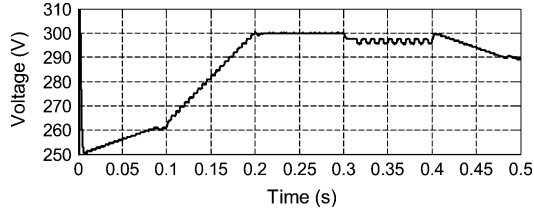


Fig. 11. The terminal voltage of the solar panel.

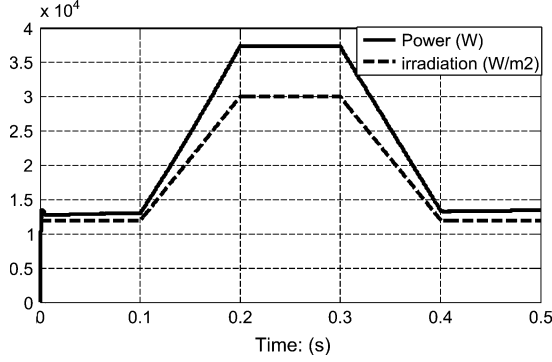


Fig. 12. PV output power versus solar irradiation.

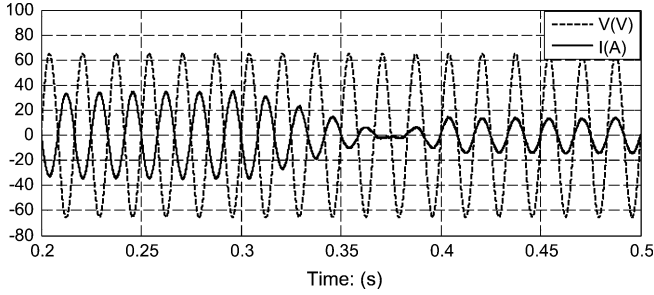


Fig. 13. AC side voltage and current of the main converter with variable solar irradiation level and constant dc load.

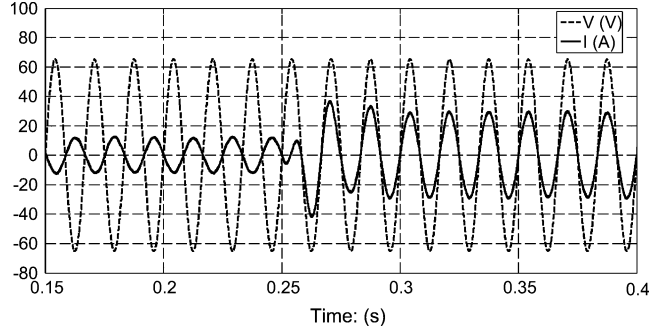


Fig. 14. AC side voltage and current of the main converter with constant solar irradiation level and variable dc load.

from the current directions that the power is injected from the dc to the ac grid before 0.3 s and reversed after 0.4 s.

Fig. 14 shows the voltage (voltage times 0.2 for comparison) and current responses at the ac side of the main converter when the dc load increases from 20 kW to 40 kW at 0.25 s with a fixed irradiation level  $750 \text{ W/m}^2$ . It can be seen from the current direction that power is injected from dc to ac grid before 0.25 s and reversed after 0.25 s. Fig. 15 shows the voltage response at dc side of the main converter under the same conditions. The figure shows that the voltage drops at 0.25 s and recovers quickly by the controller.

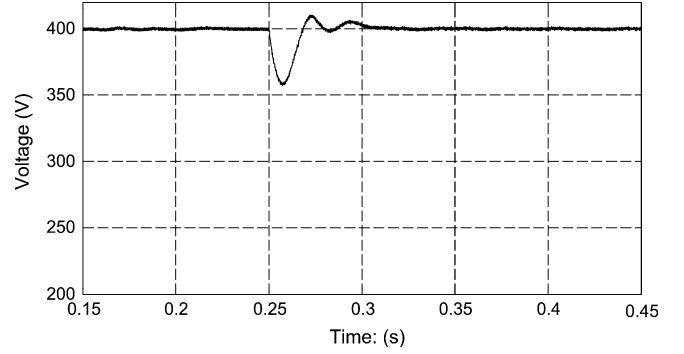


Fig. 15. DC bus voltage transient response.

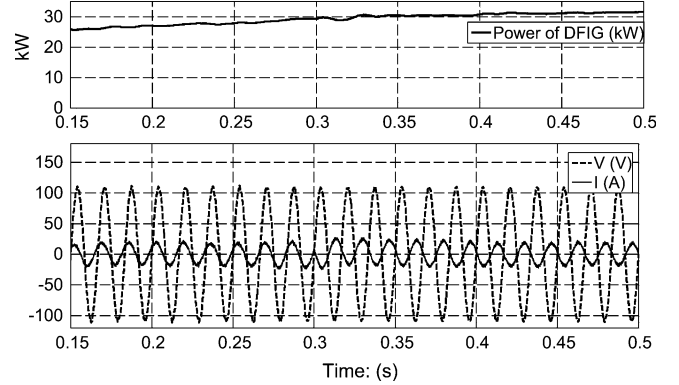


Fig. 16. Upper: output power of the DFIG; Lower: AC side voltage versus current (Voltage times 1/3 for comparison).

## B. Isolated Mode

The control strategies for the normal case and Case 1 are verified. In the normal case, dc bus voltage is maintained stable by the battery converter and ac bus voltage is provided by the main converter. The reference of dc-link voltage is set as 400 V. Fig. 16 shows the dynamic responses at the ac side of the main converter when the ac load increases from 20 kW to 40 kW at 0.3 s with a fixed wind speed 12 m/s. It is shown clearly that the ac grid injects power to the dc grid before 0.3 s and receives power from the dc grid after 0.3 s. The voltage at the ac bus is kept 326.5 V constant regardless of load conditions. The nominal voltage and rated capacity of the battery are selected as 200 V and 65 Ah respectively. Fig. 16 also shows the transient process of the DFIG power output, which becomes stable after 0.45 s due to the mechanical inertia.

Fig. 17 shows the current and SOC of the battery. Fig. 18 shows the voltage of the battery. The total power generated is greater than the total load before 0.3 s and less than the total load after 0.3 s. It can be seen from Fig. 17 that the battery operates in charging mode before 0.3 s because of the positive current and discharging mode after 0.3 s due to the negative current. The SOC increases and decreases before and after 0.3 s respectively. Fig. 18 shows that the voltage drops at 0.3 s and recovers to 400 V quickly.

When the system is at off-MPPT mode in Case 1, the dc bus voltage is maintained stable by the boost converter and ac bus voltage is provided by the main converter. Fig. 19 shows the dc bus voltage, PV output power, and battery charging current respectively when the dc load decreases from 20 kW to 10 kW at 0.2 s with a constant solar irradiation level  $1000 \text{ W/m}^2$ . The

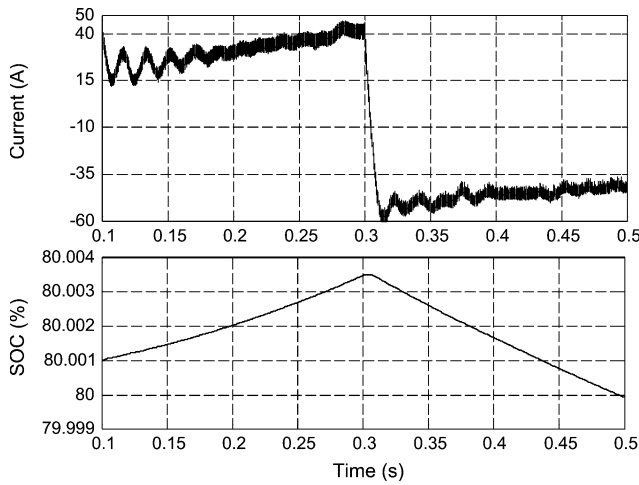


Fig. 17. Battery charging current (upper) and SOC (lower) for the normal case.

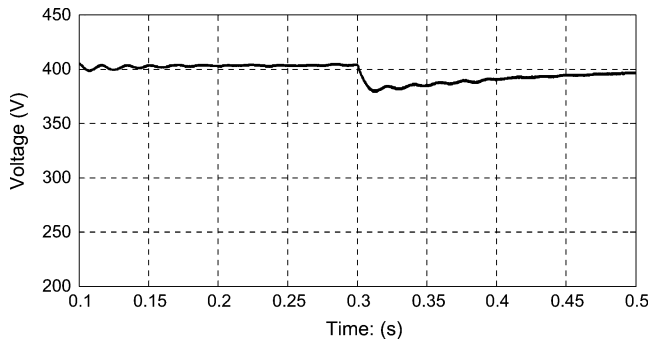


Fig. 18. DC bus voltage transient response in isolated mode.

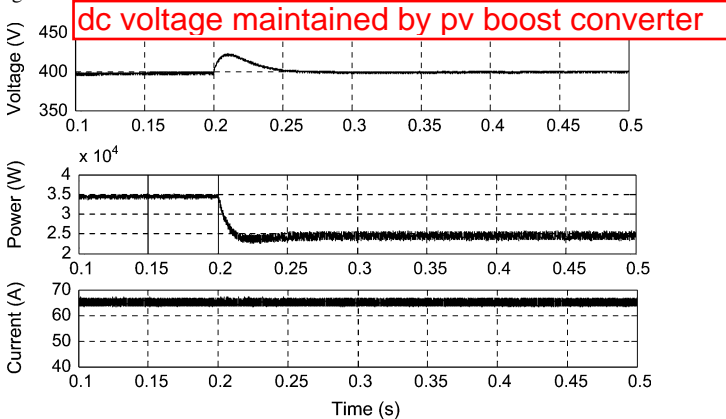


Fig. 19. DC bus voltage, PV output power, and battery current for Case 1.

battery discharging current is kept constant at 65 A. The dc bus voltage is stabilized to 400 V after 0.05 s from the load change. The PV power output drops from the maximum value after 0.2 s, which means that the operating modes are changed from MPPT to off-MPPT mode. The PV output power changes from 35 kW to 25 kW after 0.2 s.

## V. CONCLUSION

A hybrid ac/dc microgrid is proposed and comprehensively studied in this paper. The models and coordination control schemes are proposed for the all the converters to maintain stable system operation under various load and resource conditions. The coordinated control strategies are verified by

Matlab/Simulink. Various control methods have been incorporated to harness the maximum power from dc and ac sources and to coordinate the power exchange between dc and ac grid. Different resource conditions and load capacities are tested to validate the control methods. The simulation results show that the hybrid grid can operate stably in the grid-tied or isolated mode. Stable ac and dc bus voltage can be guaranteed when the operating conditions or load capacities change in the two modes. The power is smoothly transferred when load condition changes.

Although the hybrid grid can reduce the processes of dc/ac and ac/dc conversions in an individual ac or dc grid, there are many practical problems for implementing the hybrid grid based on the current ac dominated infrastructure. The total system efficiency depends on the reduction of conversion losses and the increase for an extra dc link. It is also difficult for companies to redesign their home and office products without the embedded ac/dc rectifiers although it is theoretically possible. Therefore, the hybrid grids may be implemented when some small customers want to install their own PV systems on the roofs and are willing to use LED lighting systems and EV charging systems. The hybrid grid may also be feasible for some small isolated industrial plants with both PV system and wind turbine generator as the major power supply.

## REFERENCES

- [1] R. H. Lasseter, "MicroGrids," in *Proc. IEEE Power Eng. Soc. Winter Meet.*, Jan. 2002, vol. 1, pp. 305–308.
- [2] Y. Zoka, H. Sasaki, N. Yorino, K. Kawahara, and C. C. Liu, "An interaction problem of distributed generators installed in a MicroGrid," in *Proc. IEEE Elect. Utility Deregulation, Restructuring, Power Technol.*, Apr. 2004, vol. 2, pp. 795–799.
- [3] R. H. Lasseter and P. Paigi, "Microgrid: A conceptual solution," in *Proc. IEEE 35th PESC*, Jun. 2004, vol. 6, pp. 4285–4290.
- [4] C. K. Sao and P. W. Lehn, "Control and power management of converter fed MicroGrids," *IEEE Trans. Power Syst.*, vol. 23, no. 3, pp. 1088–1098, Aug. 2008.
- [5] T. Logenthiran, D. Srinivasan, and D. Wong, "Multi-agent coordination for DER in MicroGrid," in *Proc. IEEE Int. Conf. Sustainable Energy Technol.*, Nov. 2008, pp. 77–82.
- [6] M. E. Baran and N. R. Mahajan, "DC distribution for industrial systems: Opportunities and challenges," *IEEE Trans. Ind. Appl.*, vol. 39, no. 6, pp. 1596–1601, Nov. 2003.
- [7] Y. Ito, Z. Yang, and H. Akagi, "DC micro-grid based distribution power generation system," in *Proc. IEEE Int. Power Electron. Motion Control Conf.*, Aug. 2004, vol. 3, pp. 1740–1745.
- [8] A. Sannino, G. Postiglione, and M. H. J. Bollen, "Feasibility of a DC network for commercial facilities," *IEEE Trans. Ind. Appl.*, vol. 39, no. 5, pp. 1409–1507, Sep. 2003.
- [9] D. J. Hammerstrom, "AC versus DC distribution systems-did we get it right?," in *Proc. IEEE Power Eng. Soc. Gen. Meet.*, Jun. 2007, pp. 1–5.
- [10] D. Salomonsson and A. Sannino, "Low-voltage DC distribution system for commercial power systems with sensitive electronic loads," *IEEE Trans. Power Del.*, vol. 22, no. 3, pp. 1620–1627, Jul. 2007.
- [11] M. E. Ropp and S. Gonzalez, "Development of a MATLAB/simulink model of a single-phase grid-connected photovoltaic system," *IEEE Trans. Energy Conv.*, vol. 24, no. 1, pp. 195–202, Mar. 2009.
- [12] K. H. Chao, C. J. Li, and S. H. Ho, "Modeling and fault simulation of photovoltaic generation systems using circuit-based model," in *Proc. IEEE Int. Conf. Sustainable Energy Technol.*, Nov. 2008, pp. 290–294.
- [13] O. Tremblay, L. A. Dessaint, and A. I. Dekkiche, "A generic battery model for the dynamic simulation of hybrid electric vehicles," in *Proc. IEEE Veh. Power Propulsion Conf. (VPPC 2007)*, pp. 284–289.
- [14] D. W. Zhi and L. Xu, "Direct power control of DFIG with constant switching frequency and improved transient performance," *IEEE Trans. Energy Conv.*, vol. 22, no. 1, pp. 110–118, Mar. 2007.



- [15] L. Bo and M. Shahidehpour, "Short-term scheduling of battery in a grid-connected PV/battery system," *IEEE Trans. Power Syst.*, vol. 20, no. 2, pp. 1053–1061, May 2005.
- [16] S. A. Daniel and N. AmmasaiGounden, "A novel hybrid isolated generating system based on PV fed inverter-assisted wind-driven induction generators," *IEEE Trans. Energy Conv.*, vol. 19, no. 2, pp. 416–422, Jun. 2004.
- [17] C. Wang and M. H. Nehrir, "Power management of a stand-alone wind/photovoltaic/fuel cell energy system," *IEEE Trans. Energy Conv.*, vol. 23, no. 3, pp. 957–967, Sep. 2008.
- [18] L. Jong-Lick and C. Chin-Hua, "Small-signal modeling and control of ZVT-PWM boost converters," *IEEE Trans. Power Electron.*, vol. 18, no. 1, pp. 2–10, Jan. 2003.
- [19] Y. Sozer and D. A. Torrey, "Modeling and control of utility interactive inverters," *IEEE Trans. Power Electron.*, vol. 24, no. 11, pp. 2475–2483, Nov. 2009.
- [20] N. Kroutikova, C. A. Hernandez-Aramburo, and T. C. Green, "State-space model of grid-connected inverters under current control mode," *IET Elect. Power Appl.*, vol. 1, no. 3, pp. 329–338, 2007.
- [21] F. Liu, S. Duan, F. Liu, B. Liu, and Y. Kang, "A variable step size INC MPPT method for PV systems," *IEEE Trans. Ind. Electron.*, vol. 55, no. 7, pp. 2622–2628, Jul. 2008.
- [22] D. Sera, R. Teodorescu, J. Hantschel, and M. Knoll, "Optimized maximum power point tracker for fast-changing environmental conditions," *IEEE Trans. Ind. Electron.*, vol. 55, no. 7, pp. 2629–2637, Jul. 2008.
- [23] B. Bryant and M. K. Kazimierczuk, "Voltage loop of boost PWM DC-DC converters with peak current-mode control," *IEEE Trans. Circuits Syst. I, Reg. Papers*, vol. 53, no. 1, pp. 99–105, Jan. 2006.
- [24] S. Arnalte, J. C. Burgos, and J. L. Rodriguez-amenedo, "Direct torque control of a doubly-fed induction generator for variable speed wind turbines," *Elect. Power Compon. Syst.*, vol. 30, no. 2, pp. 199–216, Feb. 2002.
- [25] W. S. Kim, S. T. Jou, K. B. Lee, and S. Watkins, "Direct power control of a doubly fed induction generator with a fixed switching frequency," in *Proc. IEEE Ind. Appl. Soc. Annu. Meet.*, Oct. 2008, pp. 1–9.
- [26] E. Koutroulis and K. Kalaitzakis, "Design of a maximum power tracking system for wind-energy-conversion applications," *IEEE Trans. Ind. Electron.*, vol. 53, no. 2, pp. 486–494, Apr. 2006.
- [27] A. H. Anbuky and P. E. Pascoe, "VRLA battery state-of-charge estimation in telecommunication power systems," *IEEE Trans. Ind. Electron.*, vol. 47, no. 3, pp. 565–573, Jun. 2000.
- [28] K. Kutluay, Y. Cadirci, Y. S. Ozkazanc, and I. Cadirci, "A new online state-of-charge estimation and monitoring system for sealed lead-acid batteries in telecommunication power supplies," *IEEE Trans. Ind. Electron.*, vol. 52, no. 5, pp. 1315–1327, Oct. 2005.
- [29] K. Kyung-Hwan, P. Nam-Joo, and H. Dong-Seok, "Advanced synchronous reference frame controller for three-phase UPS powering unbalanced and nonlinear loads," in *Proc. Power Electron. Specialists Conf.*, 2005, pp. 1699–1704.
- [30] P. C. Loh, M. J. Newman, D. N. Zmood, and D. G. Holmes, "A comparative analysis of multiloop voltage regulation strategies for single and three-phase UPS systems," *IEEE Trans. Power Electron.*, vol. 18, no. 5, pp. 1176–1185, Sep. 2003.
- [31] L. A. C. Lopes and H. Sun, "Performance assessment of active frequency drifting islanding detection methods," *IEEE Trans. Energy Conv.*, vol. 21, no. 1, pp. 171–180, Mar. 2006.
- [32] T. T. Ma, "Novel voltage stability constrained positive feedback anti-islanding algorithms for the inverter-based distributed generator systems," *IET Renewable Power Gener.*, vol. 4, no. 2, pp. 176–185, 2010.

**Xiong Liu** received the B.E. and M.Sc. degree from Huazhong University of Science and Technology, Wuhan, China, in 2006 and 2008 respectively, both in electrical engineering. He is currently working toward the Ph.D. degree in the Department of Power Engineering, Nanyang Technological University, Singapore.

**Peng Wang** (M'00) received his B.Sc. degree from Xian Jiaotong University, China, in 1978, the M. Sc. degree from Taiyuan University of Technology, China, in 1987 and the M.Sc. and Ph.D. degrees from the University of Saskatchewan, Canada, in 1995 and 1998, respectively.

Currently, he is an Associate Professor at Nanyang Technological University, Singapore.

**Poh Chiang Loh** (S'01-M'04) received the B.Eng. (Hons.) and M.Eng. degrees from the National University of Singapore in 1998 and 2000, respectively, and the Ph.D. degree from Monash University, Australia, in 2002, all in electrical engineering.

Since 2003, he has been an Assistant and Associate Professor with the Nanyang Technological University, Singapore.